Silicon Strip Detector Reconstruction Chain for the STAR Experiment

STAR NOTE 0427

B. Hippolyte, C. Kuhn, C. Suire, L. Arnold, J. Baudot, D. Bonnet, J-P.Coffin, M. Germain, C. Gojak, J-R. Lutz, A. Tarchini

Institut de Recherches Subatomiques IReS - IN2P3/CNRS - ULP
BP28, F 67037 Strasbourg Cedex 02 - France

W. Pinganau

Laboratoire SUBATECH, Université de Nantes - Ecole des Mines de Nantes - IN2P3/CNRS, 4 rue Alfred Kastler, La Chantrerie, F 44070 Nantes Cedex 03 - France

Abstract

The Silicon Strip Detector (SSD) software developped for the STAR experiment is presented. It contains three main parts, namely the simulation, the reconstruction and the evaluation modules, described in this work with emphasis on the cluster finding and the cluster matching algorithms. Their capability to solve hit ambiguities is highlighted. The efficiency and the purity of the reconstruction chain have been studied as a function of various parameters: the noise level, the rate of dead strips and the detector occupancy. Spatial and energy resolutions obtained with our methods are also presented.

Introduction

In the framework of the global data processing software of STAR, we have developed the data reconstruction chain (on the basis of C++ routines in the ROOT4STAR environment) for the 320 double-sided Silicon Strip Detectors (SSD) which compose the 4^{th} layer of the Silicon Vertex Tracker (SVT) [1]. The geometry, used in the simulation and the reconstruction, is implemented into GSTAR[1]. The detectors of the SSD barrel are positioned on 20 ladders by set of 16 modules per ladder. Each of these sensors has a rectangular shape corresponding to an overall area of $75 \times 42\,mm^2$ and a thickness of $300\,\mu m$. On each side, 768 micro-strips are implanted with a pitch of $95\,\mu m$. The strips are $40\,mm$ long and tilted by an angle of $17.5\,mrad$ with respect to the short side of the detector [2]. The centers of the detectors are at a radius of $230\,mm$ from the interaction point. The simulated performances of the detectors and of the read-out electronics, especially of the ALICE 128C chip, are extrapolated from in- and off-beam test measurements [3] [4].

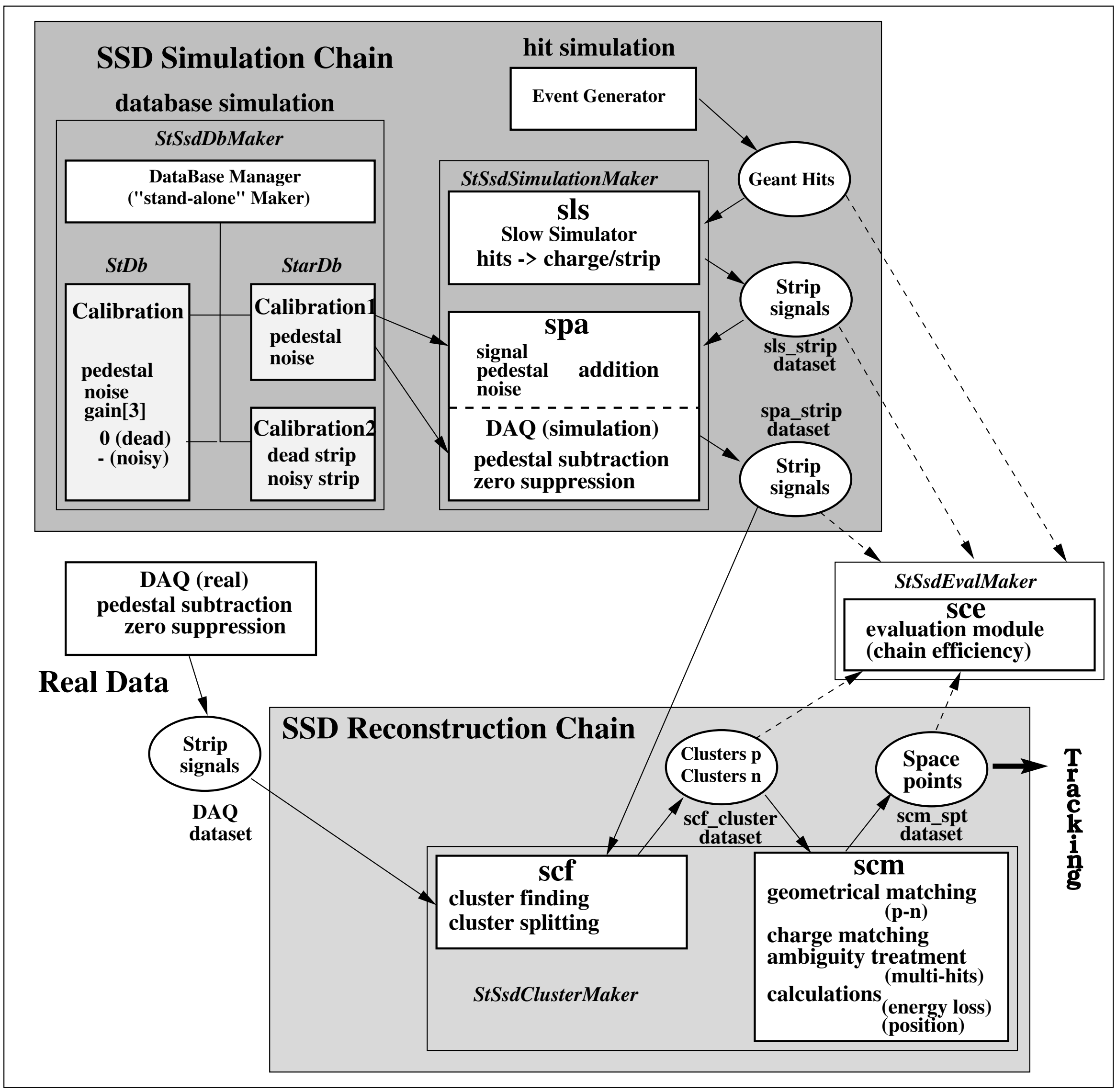

Figure 1: SSD Simulation and Reconstruction chains

[1] star GEANT

The organisation of the SSD reconstruction chain is schematically shown in Fig.1 together with the SSD simulation chain. Each module, respectively *StSsdClusterMaker* and *StSsdSimulationMaker*, contains its specific Makers and C++ PAMs [2].
The first task (PAM **scf**) of the reconstruction part is to scan the strip-signals on both sides of each double-sided micro-strip detector in order to build the clusters. The second step (PAM **scm**) consists in identifying the geometrical correspondences between the p-side and the n-side clusters, which allows to find the space points and to determine both their position and their associated energy loss. Depending on the hit positions on the detector, these geometrical associations can be not trivial and lead to ambiguous situations (correlations between several clusters of each side). A strategy based on charge-matching is applied to select the correct space point configurations. Indeed for a given particle, the charges collected on both sides of the detector are produced by the same energy deposit. These cluster finding and matching algorithms will have to process the real data (pedestal subtracted and zero suppressed data) given by the DAQ. They are tested using simulated data produced by the **sls** et **spa** PAMs of the SSD simulation chain (also drawn in Fig.1).
Moreover, for simulation purposes, one can generate and modify the reconstruction parameters and calibration data (for instance, number of dead or noisy strips, noise conditions...) with a dedicated module (*StSsdDbMaker*) and store these information either into the database (*StDb*, depending on user's privileges) or locally (*StarDb*, as ROOT files). The results coming out of the reconstruction chain are checked and evaluated by a specific PAM (**sce**).

1 Simulation

The input of the simulation consists of events generated by HIJING (parton cascade model). Then, by using GSTAR, one gets the impact positions of the particles and their energy deposit. With this information, the SSD Lazy Simulator (**sls**) transforms the GEANT hits into sequences of strips, each being attributed a fraction of the energy deposit. First of all, it converts the coordinates of the hits to the local reference frame (according to the strip orientation and defined as (x_l, y_l)) of each detector and removes hits in inactive areas. Then, it simulates the charge collection in the silicon and the charge sharing between the micro-strips by using different factors for diffusion and induction (due to strip-to-strip capacitance). It finally performs an analog-digital conversion.

This leads to clusters of strips with various sizes (between 1 and 5 strips), according to a function obtained from a fit to experimental distributions [5]. The **sls** PAM still needs improvements such as the dependence of the amplitude with respect to the incident angle of the particle and the non-uniform energy loss through the material. At the end, an output dataset (sls-strip-signal table) is fulfilled with the charge (ADC counts) of all the fired strips.

Characteristics	Nominal (e^-)
mean value of strip P noise	700
mean value of strip N noise	1100
dispersion of strip P noise	50
dispersion of strip N noise	70
percentage of dead strips	1

Table 1: Simulated noise and dead strip rate, extrapolated from beam test measurements.

[2] Physics Analysis Module

Besides, a mean noise and a pedestal value are generated for each strip-channel by the *StSsdDbMaker* module, which stores these information into a calibration database. This module gives also the information about the state (i.e. active or dead) of each strip. The nominal values of the noise and of the pedestal as well as the number of dead strips are built according to sets of parameters derived from measurements of double-sided Si-strip detector prototypes and their electronics, performed during beam (CERN SPS) tests [3] [4] (see Tab.1). They will be varied in order to study the influence of noise and/or dead strips on the reconstruction efficiency (see sections 2.1 and 3.2). The noise and pedestal simulation is illustrated in Fig.2.

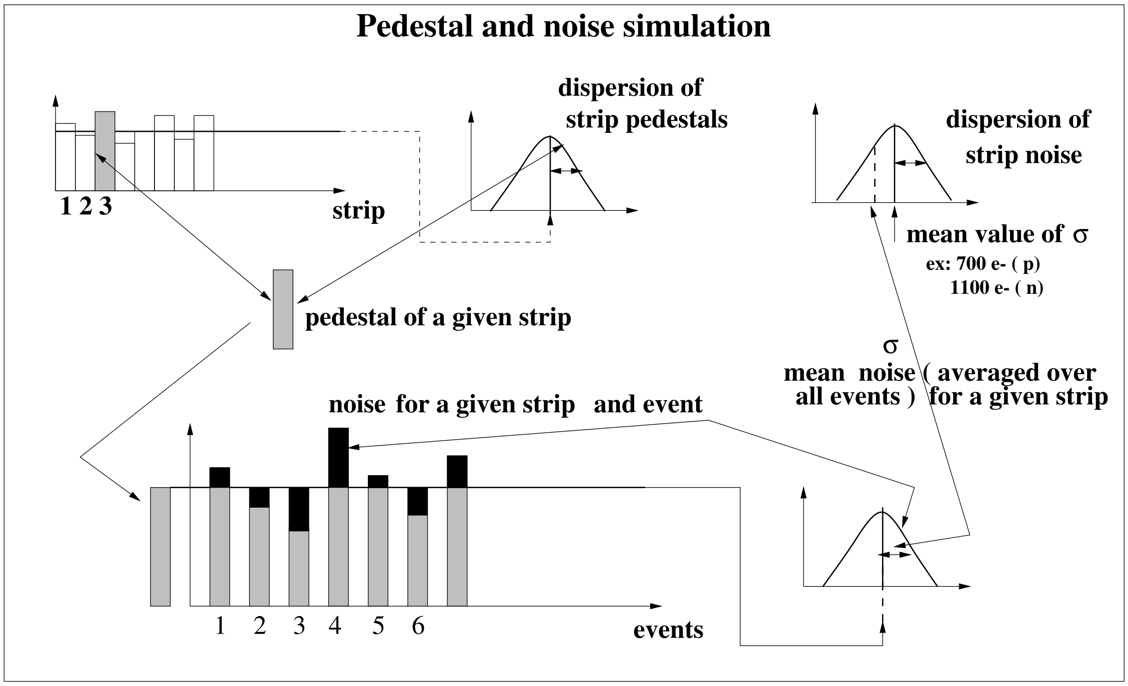

Figure 2: Pedestal and noise simulation.

The calibration database is then used by the SSD Pedestal Annihilator (**spa**) PAM to simulate real data on each strip: pedestal + noise + physics signal (when fired) from **sls**. The **spa** has also to simulate the behavior of the DAQ : pedestal subtraction and zero suppression (only the strips having a signal over noise ratio S/N larger than 4 are retained).
The remaining data are stored in the spa-strip-signal dataset which is then read by the reconstruction routines. This table contains the identification number of those strips and their ADC count value. The **spa** needs to be updated in order to include the 10 to 8 bits data compression performed by the DAQ.

2 Reconstruction

2.1 Cluster finding procedure

In order to identify the clusters of strips, on both side p and n of the detectors, the task of the SSD Cluster Finder (**scf**) algorithms consists in finding their "central" strip and corresponding neighbouring strips. The central strip is defined as the one which has collected the maximum charge. For nominal values of noise, i.e. 700 e^- on the p-side (1100 e^- on n-side), which gives a mean cluster S/N of about 56

on p-side (29 on n-side) for MIP particles (25000 e^- produced in 300 μm of silicon), the S/N cut that we have applied on the signal of the central strips with the best efficiency and purity compromise is equal to 5.
This threshold is of course dependent on the noise amplitude. Note that the S/N of a cluster is defined by the following formula:

$$S/N = \frac{\text{sum of the strips ADC count values}}{\text{mean noise of the cluster}}.$$

The mean noise of the cluster is the average of the noise of each strip contained in the cluster.
Once the clusters have been found, one looks, according to shape criteria (typically one or several local minima in the cluster profile), for the ones that may be split because they hide a double -or multi- hit. HIJInG events produce a mean value of particles per event of about 5 (exactly 5.4) per SSD detector for an hadronic cocktail with a standard density. The mean number of cluster per detector and per side is approximatively the same.
At the end of this procedure, the information about each cluster is, on one hand, saved in a ROOT file used for evaluation and, on the other hand, transmitted to the next Maker in a table described in Tab.2.

• cluster address
• first strip
• number of strips
• sum of strip ADC count values
• ADC count value of the first strip in the cluster
• ADC count value of the last strip in the cluster
• sum of strip-noise values
• center of gravity of the cluster
• flag (split cluster)

Table 2: SCF-cluster table content.

Besides, QA histograms are generated by **scf** in order to check some characteristics of the reconstructed clusters e.g. the distribution of the S/N ratio:

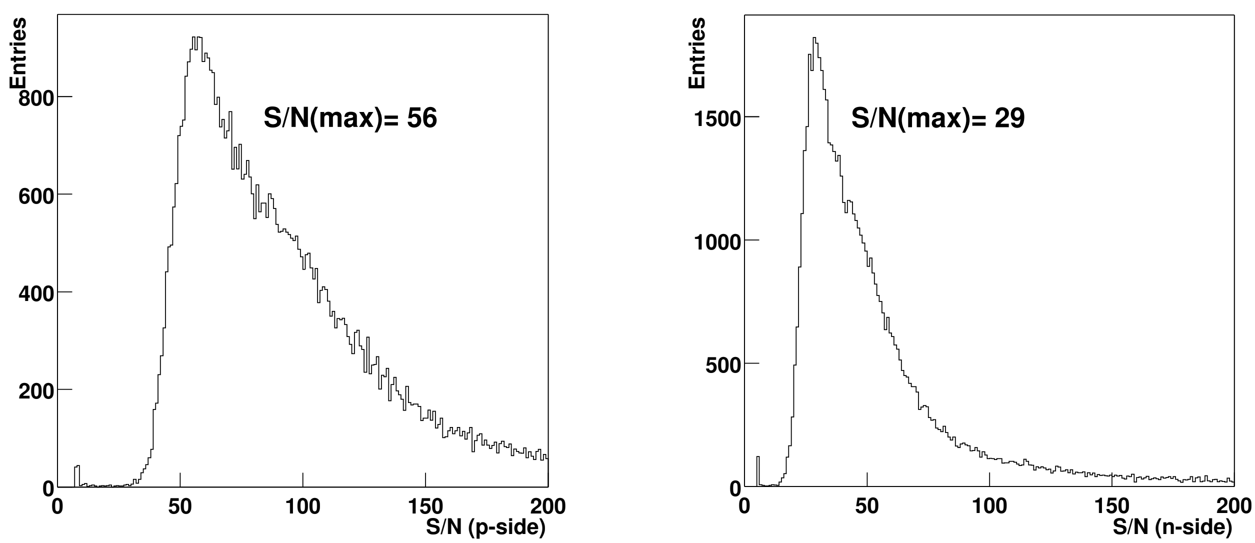

Figure 3: S/N ratio for nominal noise (both sides), no dead strips, DAQ cut = 4 and **scf** cut = 5 .

The DAQ cut can be adjusted in order to minimize the number of ghost clusters depending on the noise. The cluster S/N distributions, as obtained with our method (with a statistic of 40 standard hadronic cocktail events) for nominal noise values, are shown in Fig.3 and can be compared with those corresponding to other conditions of noise and numbers of dead strips, as shown in Tab.3.

Characteristics		DAQ cut	**scf** cut	S/N(max)	Efficiency	Purity
A	p	4	5	56	98.8%	99.9%
	n	4	5	29	98.8%	99.8%
B	p	4	5	56	96.1%	99.9%
	n	4	5	29	95.5%	99.4%
C	p	3	4	9	97.0%	98.6%
	n	3	4	6	84.8%	99.2%
D	p	3	4	9	92.8%	98.6%
	n	3	4	6	80.9%	99.2%
E	p	2	3	9	98.4%	78.8%
	n	2	3	6	93.7%	81.7%
F	p	2.5	3.5	9	98.0%	92.7%
	n	2.5	3.5	5	89.8%	95.6%

Table 3: Reconstruction results for different noise and dead strip rate conditions.

The characteristics A,B,C,D,E, and F correspond to noise conditions and dead strip rate explicited below:

A) noise of $700e^{-}/1100e^{-}$ (sides p/n) and no dead strip.
B) noise of $700e^{-}/1100e^{-}$ (sides p/n) and 5% of dead strips.
C,E,F) noise of $3500e^{-}/5500e^{-}$ (sides p/n) and no dead strip.
D) noise of $3500e^{-}/5500e^{-}$ (sides p/n) and 5% of dead strips.

And where:

Efficiency = NT/NS
Purity = NT/(NT + NG)

NS = SIMULATED clusters
NT = TRUE reconstructed clusters
NG = GHOST clusters

The noise values of 3500 e^{-} (p-side) and 5500 e^{-} (n-side), which represent a noise level five times larger than the nominal one, correspond, according to irradiation tests performed at IReS [7], to the very pessimistic case of detectors receiving a dose of more than 300 Krad, which is far above the irradiation level expected at RHIC for the SVT [8]. For these high noise conditions, the DAQ cut and the **scf** cut have to be lowered to keep a reasonable efficiency. According to Tab.3, the best compromise seems to be 3-4 (case C) or even 2.5-3.5 (case F). By using smaller values (like case E), the efficiency could still be enhanced but would lead to a too high level of contamination (ghosts).

The variation of the efficiency and of the purity is shown in Fig.4 as a function of the **scf** cut for a fixed DAQ threshold (3).

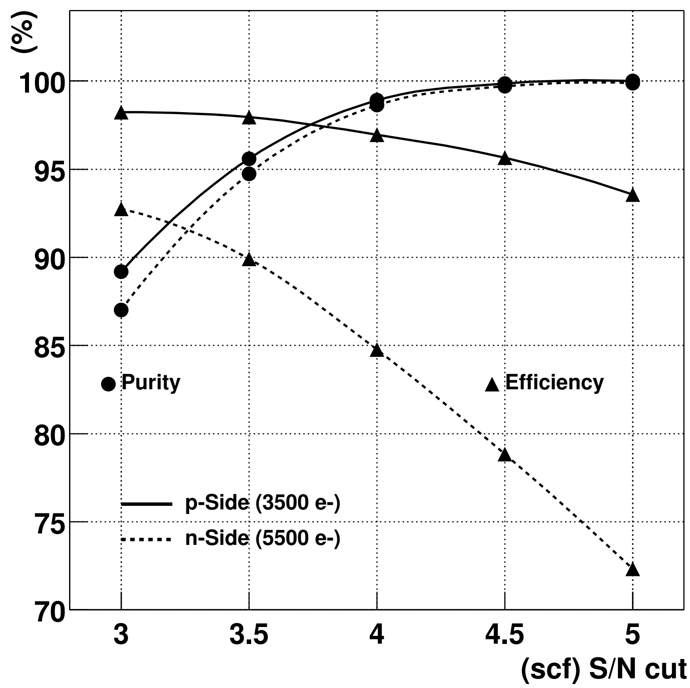

Figure 4: Efficiency and Purity as S/N cut dependent ($\mathrm{DAQ}_{threshold}$=3) for a high level of noise (nominal noise $\times$ 5).

It is expected that the contribution of noisy strips will lead to a loss of purity proportional to their rate, similarly to the loss of efficiency due to dead strips. Nevertheless we will also randomly introduce a given number ($5-10\%$) of very noisy strips in order to study their effect on the reconstruction.

2.2 Cluster geometrical matching

After the **scf** treatment, one has a list of p-clusters and a list of n-clusters for each detector. The first task of the SSD Cluster Matching (**scm**) PAM is to find the correct geometrical associations between them in order to determine the particle impact points (space points). The method is schematically shown in Fig.5.

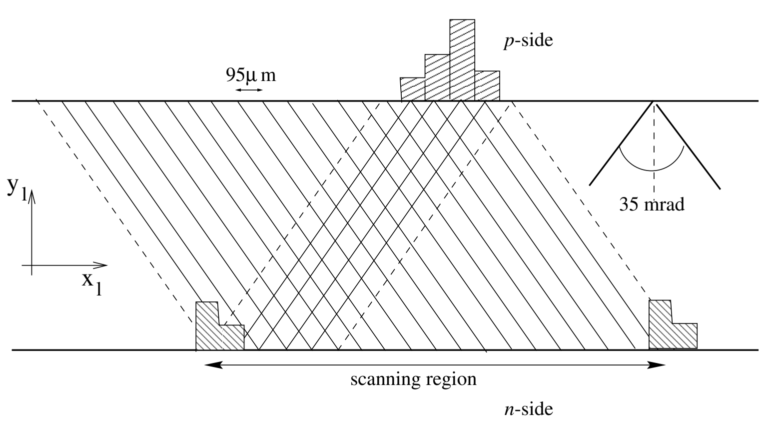

Figure 5: Example of a geometrical association between one p-cluster and two n-clusters.

Starting, for example, with a cluster on the p-side (as shown on the drawing) and knowing its topology (first and last strip), one looks for the corresponding n-side clusters in a well defined geometrical region. This region contains all the n-side strips which cross the strips of the p-side cluster (each strip of one side crosses 16 strips of the other side).
By repeating this procedure for each p and n-side cluster, one is able to find all the possible links (i.e. crosses) between them and hence to define well separated groups of geometrically matched p and n clusters, named *cluster-packages*, for each detector.

The mean number of particles per detector being of about 5 and 10, for respectively standard and high density, the number of cluster-packages with more than one p and one n-cluster involved is not negligible: about 14% for standard density and more than 28% for the high one.

Two examples of cluster-packages, which may be identified on a detector, are drawn in Fig.6. The first example is the trivial 1-1 association which represents the most probable case (about 86% for standard and 72% for high density): a single p-cluster ($1p$) linked to a single n-cluster ($1n$). This leads to one non ambiguous space point. The second package contains 2 p-clusters and 2 n-clusters. Each p-cluster ($1p$, $2p$) is linked with 2 n-clusters ($1n$, $2n$) and vice and versa (the links are represented by the arrows in Fig.6. In this so called 2-2 case, there are 4 possible space points (4 crosses) but only two of them are real: the two others are ghosts. The method used to distinguish between the ghosts and the real ones is described in the next section.

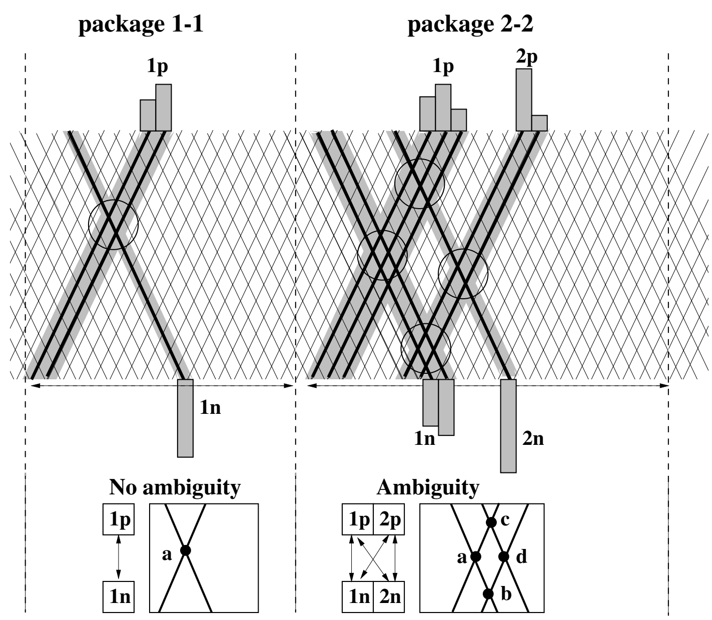

Figure 6: Example of unambiguous and ambiguous cluster-packages

If we limit ourselves to packages containing a maximum of 6 clusters (i.e. 3 by 3), which allows us for solving more than 99% of the space points for standard density, all the situations (i.e. 1-1, 1-2, 1-3, 2-2, 2-3, 3-3 associations with their various possible geometric configurations: links symbolized by the arrows) are summarized in Fig.7 with their associated frequency.
However, the recent study of the occurrences related to high multiplicity events may indicate that the treatment of cases up to 4-4 would improve the global efficiency for such events.

For the cases 1-1, 1-2, 1-3 and 2-2A, as shown in Fig.7 and Fig.8, there is no ambiguity due to geometric overlap. Hence, the space point positions (given by the crosses) and the corresponding energy loss can be determined with a reasonable level of confidence (see results of the evaluation in section 3).

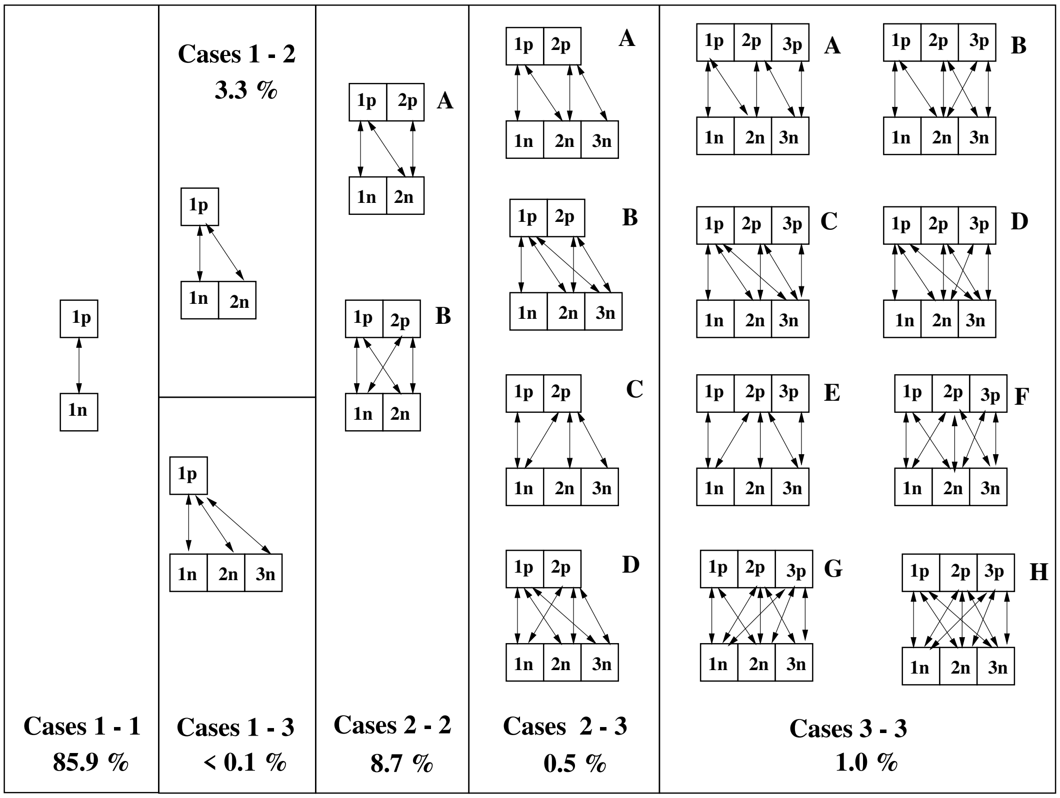

Figure 7: Cluster-packages (clusters associations and geometrical configurations) and occurrences for HIJInG standard events.

In case 1-1, the energy loss of the space point a is given by:

$$dE_a = \frac{(dE_{1p} + dE_{1n})}{2}$$

where:

- dE_{1p}: energy deposit of the p-side;
- dE_{1n}: energy deposit of the n-side.

Nevertheless, in cases such as $1-2$ where there are two space points a and b, two possibilities can be compared:

$$\begin{aligned} dE_a &= dE_{1n} \\ dE_b &= dE_{2n} \end{aligned}$$

or

$$\begin{aligned} dE_a &= \frac{(dE_{1p} - dE_{2n}) + dE_{1n}}{2} \\ dE_b &= \frac{(dE_{1p} - dE_{1n}) + dE_{2n}}{2} \end{aligned}$$

where:

- dE_{1p} : energy deposit of the p-cluster;
- dE_{1n} : energy deposit of the first n-cluster;
- dE_{2n} : energy deposit of the second n-cluster.

In the first possibility, as the energy deposit on the p-side corresponds to 2 n-clusters, we only use the non ambiguous energy deposit of the n-clusters to find the energy of the space points but the information of the p-side energy deposit is lost.
The second possibility, the one implemented, shares the variation of the noise between the p-side and the n-side: the information of the energy deposit on both sides are used.
For the treatment of the case 1-3 and for the much more complex cases, the same choice has been made:

$$\begin{aligned} dE_a &= dE_{1n} \\ dE_b &= dE_{2n} \\ dE_c &= dE_{3n} \end{aligned} \qquad \text{or} \qquad \begin{aligned} dE_a &= \frac{(dE_{1p} - dE_{2n} - dE_{3n}) + dE_{1n}}{2} \\ dE_b &= \frac{(dE_{1p} - dE_{1n} - dE_{3n}) + dE_{2n}}{2} \\ dE_c &= \frac{(dE_{1p} - dE_{1n} - dE_{2n}) + dE_{3n}}{2} \end{aligned}$$

where:

- dE_{1p} : energy deposit of the p-cluster;
- dE_{1n} : energy deposit of the first n-cluster;
- dE_{2n} : energy deposit of the second n-cluster;
- dE_{3n} : energy deposit of the third n-cluster.

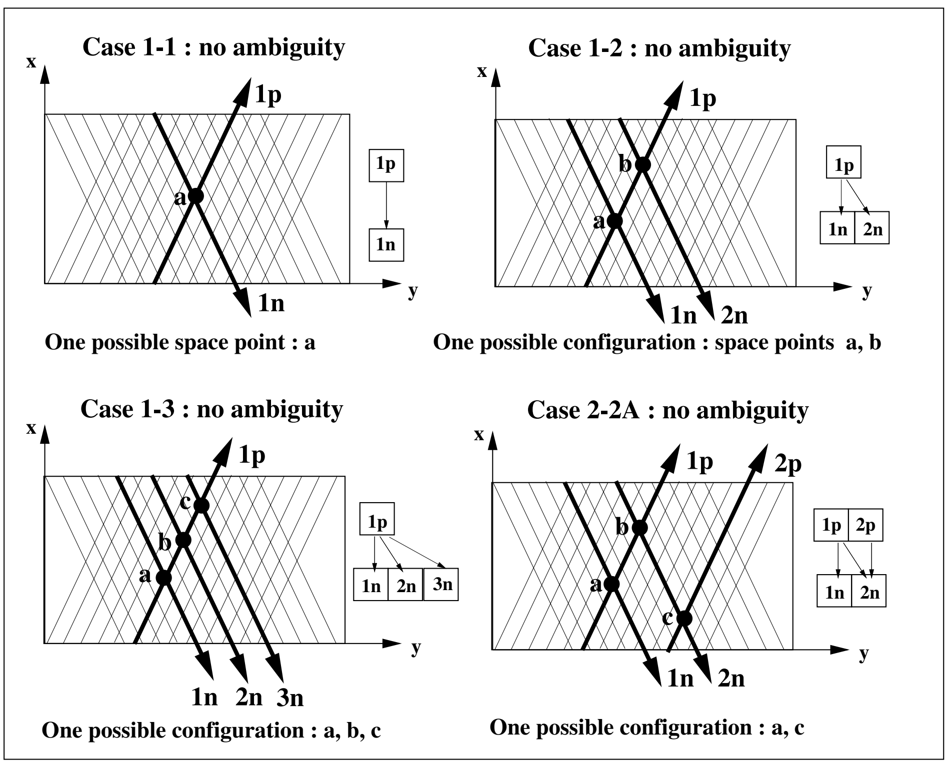

Figure 8: Unambiguous cases: a configuration leads to only one set of points.

Of course, some bias coming from dead strips (which can totally hide a cluster) or from noisy strips (which biases the signal value or even may produce ghost clusters) will decrease the reconstruction efficiency and the resolution (see section 3).

Actually, it is possible to take into account the dead and noisy strips in our treatment but it implies to make, on the basis of charge matching (see section 2.3), some assumptions on the missing charges. This development is in progress.
Moreover, we have to neglect the probability of special multi-hits (for instance 2 particles falling so close to each other that they produce together only one cluster on each side) because this situation can simply not be distinguished from a single hit with the sum of the energy deposits, except part of the cases which has already been solved by cluster splitting (see section 2.1).

For each p-n cluster association, the intersection of the lines (parallel to the strips) corresponding to the center of gravity of the p-cluster and the n-cluster respectively, gives the position of the corresponding space point. In the detector local frame, it is given by the following formula:

$$
\begin{aligned}
x_l &= \frac{(U_n + U_p)}{2} - L + W \times tan\theta. \\
y_l &= \frac{(U_n - U_p)}{2 \times tan\theta}.
\end{aligned}
$$

- U: mean position of the cluster;
- L: active length of the wafer;
- W: active width of the wafer;
- θ: stereo angle between p and n strips.

Then by using a coordinate transformation matrix, one gets the position of each space point in the global STAR frame (z parallel to the beam axis and $r\phi$ in the bending plane).

2.3 Cluster charge matching

For the cases 2-2B, 2-3 and 3-3 (Fig.7), we obtain more possible space points than real is, hence ambiguities. Among the different space point configurations, one has to choose the right one, i.e. the one which offers the best global charge matching.

Indeed, when a particle passes through a double-sided Si detector of the SSD, the same quantity of charges is collected on both sides, with some small variations due to statistical fluctuations and systematic biases due to the noise which is different from one strip (one side) to another.
Another contribution to these errors may come from the following effect: if we consider hits giving most of the signal on one strip, the fraction of signal on the neighbouring strips may be lost because it does not exceed the DAQ S/N threshold. Thus we underestimate the pulse height of such a cluster.

The charge matching distribution, obtained in the case 1-1 and shown in Fig.9 exhibits a nice correlation (along the straight line corresponding to the perfect matching) between the p and the n-side collected signals.

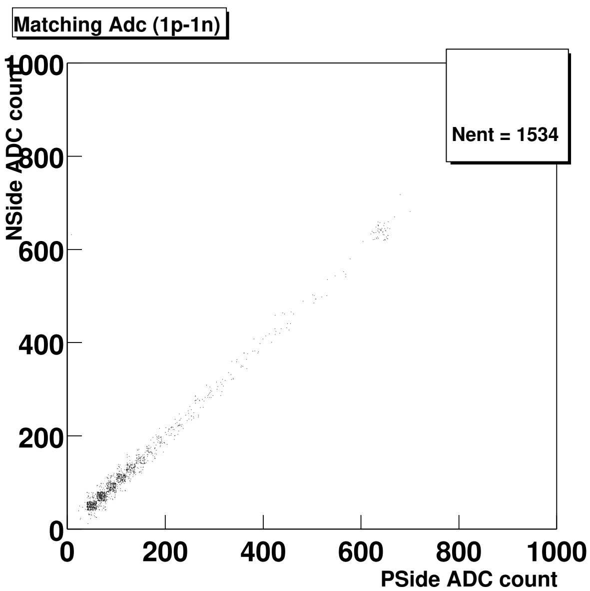

Figure 9: Charge matching distribution.

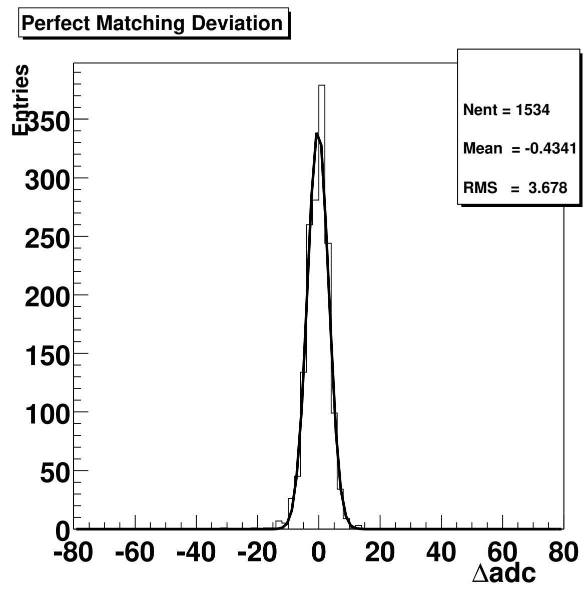

Figure 10: Orthogonal projection.

This distribution can be characterized by a standard deviation not far from 4 ADC count (Fig.10) and is used to solve the aforementioned cases:

Case 2-2B: The method used to treat this situation is illustrated in Fig.11. Here, we have 2 possible space point configurations: either **a-d** or **b-c**.

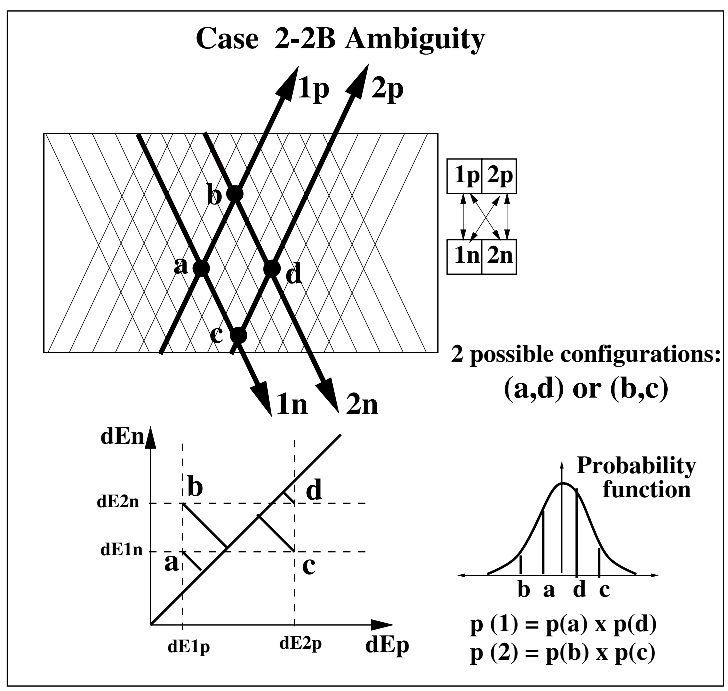

Figure 11: Using perfect matching distribution to solve case $2-2B$.

The charges (on both sides) corresponding to each space point are the following:

$$\begin{array}{ccc} \mathbf{a}(dE_{1p}, dE_{1n}) & \multirow{2}{*}{or} & \mathbf{b}(dE_{1p}, dE_{2n}) \\ \mathbf{d}(dE_{2p}, dE_{2n}) & & \mathbf{c}(dE_{2p}, dE_{1n}) \end{array}$$

Each of these couples is represented on the dE_p (charge collected on p-side) versus dE_n (n-side) diagram. By calculating the distance from these points to the perfect charge matching line, one can evaluate the relative probability of each configuration $p(1)$ and $p(2)$ using Fig.10 as reference. The configuration with the higher probability is chosen and the 2 retained space points (either **a**,**d** or **b**,**c**) can then be transmitted to the tracking, with a confidence level which is proportional to their configuration probability.

Cases 2-3: The various geometrical situations corresponding to this type of cluster-packages are represented in Fig.12. Of course, cases 3-2 (3 p-clusters and 2 n-clusters) are equivalent for obvious reasons of symmetry.

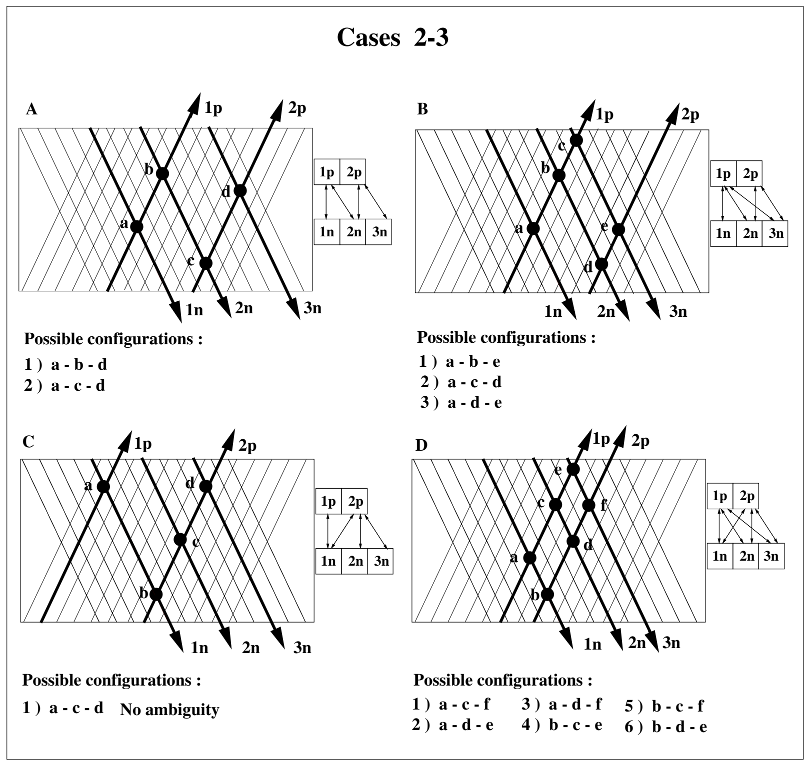

Figure 12: Situations corresponding to cases 2-3.

In each case, the possible space point configurations are listed. Note that in case 2-3C, there are no ambiguities. The treatment of the 3 others cases is the same as the one used in case 2-2B except that it is a bit more complicated because of the asymmetry between the number of clusters of the two sides.

An example, corresponding to the case 2-3A is given in Fig.13. Here, we have 2 possible configurations: 1) **a-b-d** or 2) **a-c-d**. One has to plot the couples (dE_{1p}, $dE_{1n} + dE_{2n}$) and (dE_{2p}, dE_{3n}) for configuration 1, and the couples (dE_{1p}, dE_{1n}) and (dE_{2p}, $dE_{2n} + dE_{3n}$) for configuration 2 in order to compare the relative probabilities of the two configurations.
In this particular case, note that the points **a** and **d** have a probability of 100%. The cases 2-3B and 2-3D are even more complex because one has to compare respectively 3 and 6 series of energy loss couples.

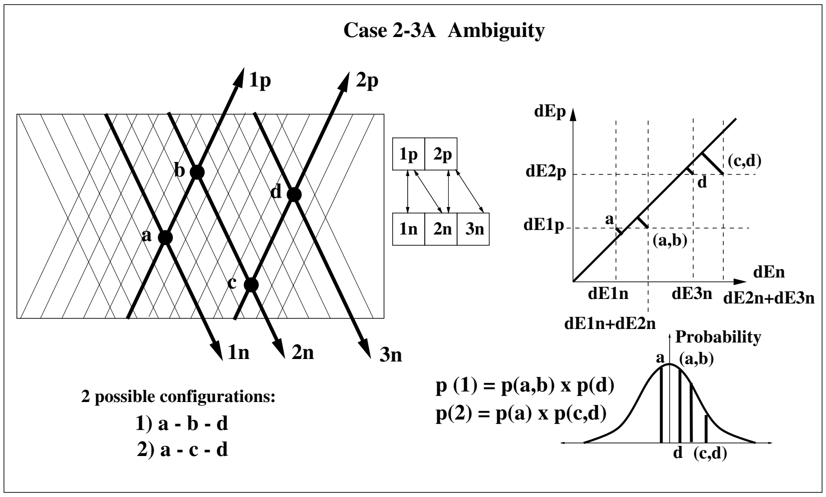

Figure 13: Configurations to check in a 2-3A case.

Cases 3 - 3: The 8 geometrical situations corresponding to such a case are shown in Fig.14.

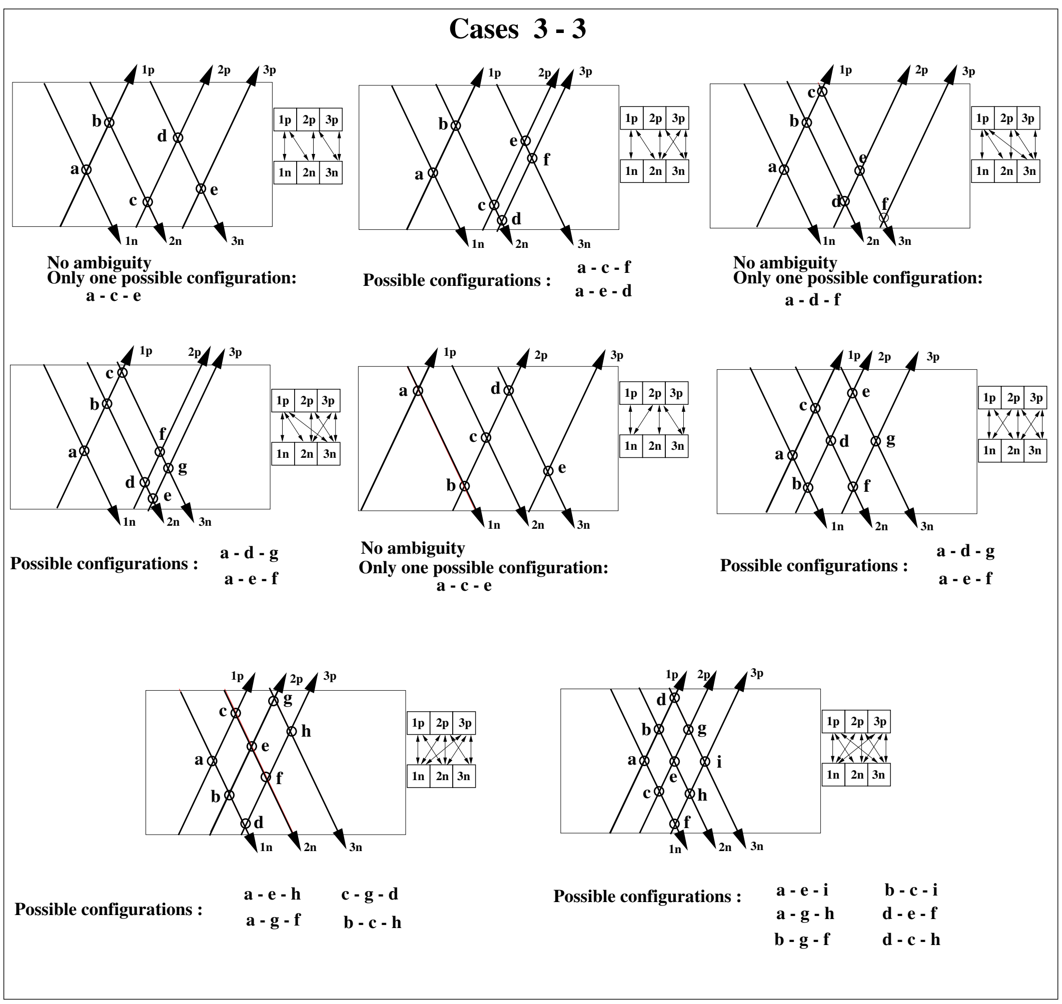

Figure 14: Geometrical situation corresponding to 3-3 case.

Thus, once the cluster geometrical matching and the ambiguity treatment are performed, space points are obtained and transmitted to the tracking where a threshold on the level of confidence can be used. The following table 4 resumes the relevant piece of information relative to each point.

- space point address
- level of confidence
- kind of package
- identifier of the wafer
- energy loss (and error)
- coordinates in wafer reference system
- coordinates in STAR reference system

Table 4: SCM-spt (space points) table content.

3 Evaluation

The evaluation of the reconstruction chain is made by a specific PAM (**sce**) which compares the results stored in the various tables (**spa-strip**, **scf-cluster**, **scm-spt**) with the initial GEANT hits. Each strip, each cluster and finally each space point are linked to their original simulated hit via a set of keys propagated from the beginning of the chain to its end.

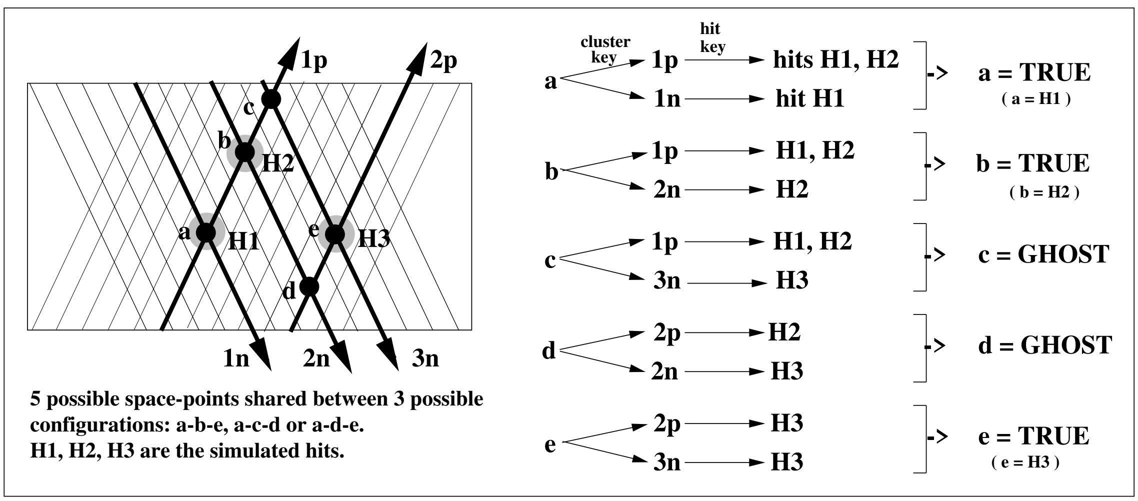

Figure 15: Links to simulated hits and example of evaluation.

An illustration of the evaluation procedure is given in Fig.15 for the case 2-3B: among the 5 reconstructed space points **a,b,c,d,e**, only three of them are TRUE. The simulated GEANT hits ($H1$,$H2$,$H3$) are also represented. Via this key system, each reconstructed space point keeps the memory of its 2 clusters (p and n). Each of these 2 clusters is linked to one or several simulated hits. If the p-cluster and the n-cluster have a common hit, then the corresponding space point is a TRUE point (this is the case for the space points **a, b, e** in the example of Fig.15). Otherwise, it is a GHOST point (space points **c,d**).
These links allow to determine how many TRUE and how many GHOST space points are reconstructed with our method. Indeed, let us consider the example shown in Fig.15: if the calculation of the configuration probabilities, as explained before, indicates that P(a-b-e) is better, we will find only TRUE space points. But if we find that P(a-c-d) or P(a-d-e) is the best, we will find, in the first case, one TRUE and two GHOST space points, and in the second case, two TRUE and one GHOST space points.

3.1 Efficiency, purity and resolution definitions

In the next sections, we will look to different relevant rates and values that need to be first of all specified. The efficiency is defined as:

$$Efficiency = \frac{\text{TRUE space points}}{\text{SIMULATED hits}}.$$

The purity is defined as:

$$Purity = \frac{\text{TRUE space points}}{\text{TRUE space points} + \text{GHOST space points}}.$$

Moreover, for each true space point, we also calculate:

- the position resolution, as the distance between its reconstructed position and the position of the corresponding simulated hit (see Fig.16).
- the energy resolution, as the relative difference between calculated and simulated energy losses (see Fig.17).

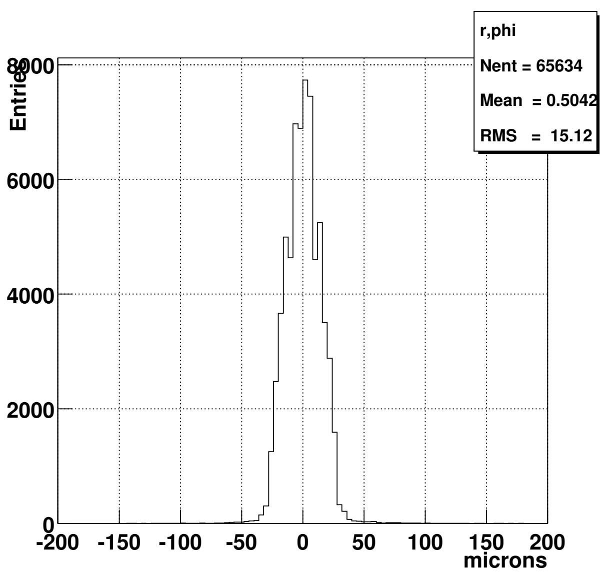

Figure 16: Position $r\phi$ resolution.

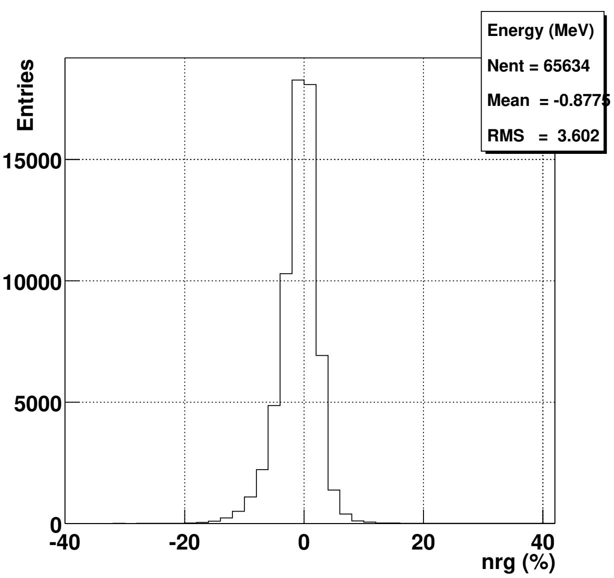

Figure 17: Energy resolution.

3.2 Consequences of dead strips and noise level

Let us now examine these quantities, for the nominal values of the noise and for a perfect detector (without dead or noisy strip). Without the treatment of cases 2-2, 2-3 and 3-3, the purity would be close to 100% but the efficiency stays rather low (90%) (see Fig.7 in 2.2). But when using our charge matching method to solve the ambiguous cases, the purity decreases to 99% but the gain in efficiency is substantial, reaching 96%.
The evolution of the global efficiency, purity and resolutions is shown in Figs. 18 to 21 as a function of the number of dead strips .

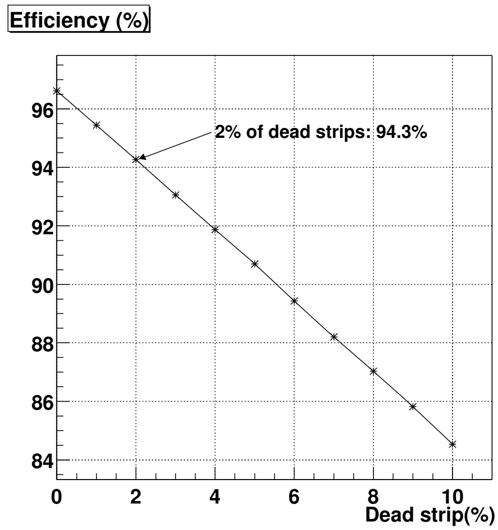

Figure 18: Global efficiency VS dead strips.

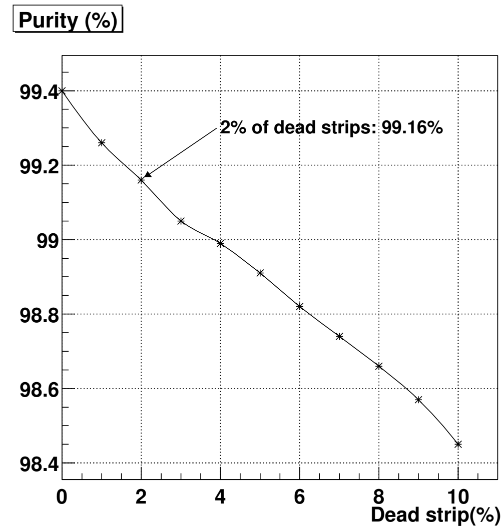

Figure 19: Global purity VS dead strips.

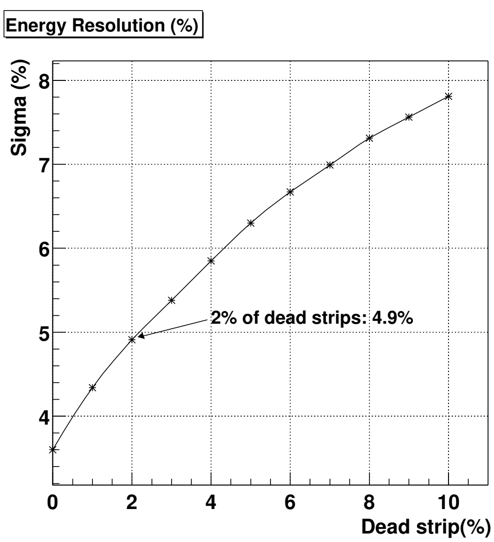

Figure 20: Energy resolution VS dead strips.

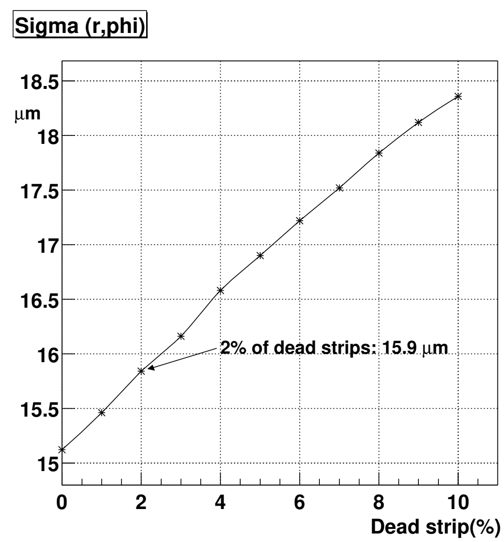

Figure 21: Position resolution VS dead strips.

One can see the incidence of dead strips which is very important for efficiency and resolutions. The nominal value for dead strips is assumed to be $\simeq 1\%$ [9] and randomly distributed as it has been simulated on the above plots.

The influence of an increasing level of noise has been studied and detailed in Figs. 22 to 25 for 0% and 2% of dead strips.

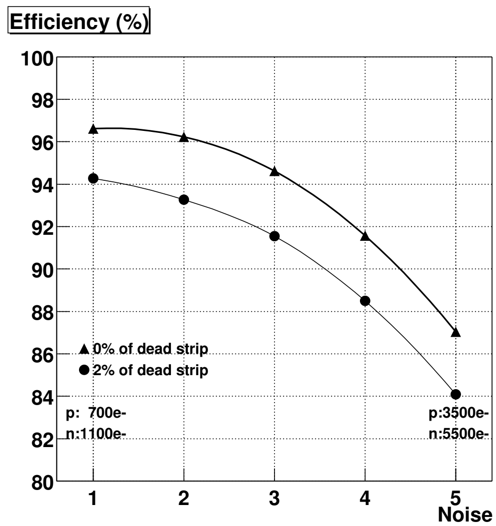

Figure 22: Global efficiency VS noise.

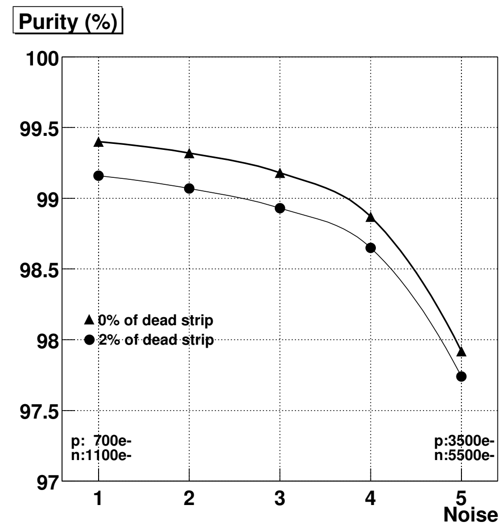

Figure 23: Global purity VS noise.

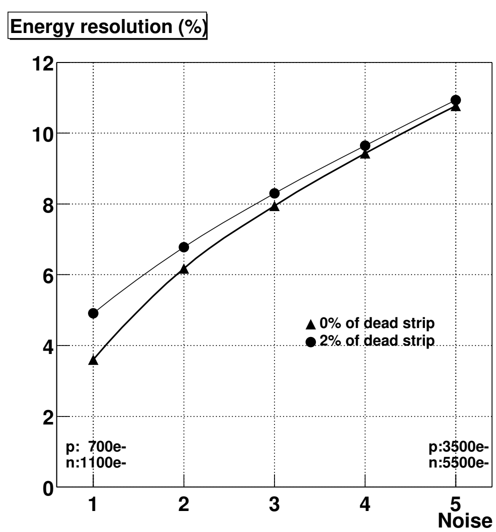

Figure 24: Energy resolution VS noise.

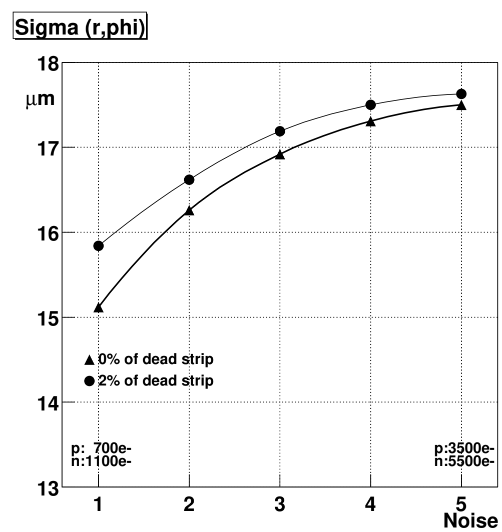

Figure 25: Position resolution VS noise.

3.3 Evaluation results for the expected multiplicity

We have performed a systematic study of these evolutions, by looking at these quantities, case by case and for different conditions of noise and defects (dead strips). For (40) standard density events with 5.4 hits on the average per detector, these information are summarized in Tab.5 and Tab.6:

Cases	Efficiency	Purity	$\sigma_{r,\phi}(\mu m)$	$\sigma_z(\mu m)$	$\sigma_{de}(\%)$
$1-1$	97.8%	99.9%	13.5	738	3.4
$1-2$	93.2%	97.8%	35	1530	6.5
$2-2$	95.3%	95.2%	18.0	790	3.9
$2-3$	78.5%	93.1%	28	1270	5.9
$3-3$	77.1%	91.9%	19	720	4.1
Global	96.7%	99.4%	15.1	780	3.6

Table 5: Evaluation results (nominal noise, no dead strip) for standard density.

Conditions	Efficiency	Purity	$\sigma_{r,\phi}(\mu m)$	$\sigma_z(\mu m)$	$\sigma_{de}(\%)$
A	96.7%	99.4%	15.1	780	3.6
B	90.7%	98.9%	16.9	870	6.3
C	81.7%	98.4%	17.6	930	10.3
D	74.8%	98.0%	18.1	950	10.7
E	90.9%	94.8%	17.7	900	11.7
F	87.4%	97.9%	17.5	910	10.6

Table 6: Evaluation results (nominal noise $\times$ 5 and deadstrips, see definitions in Tab.3) for standard density.

Then, in order to see the consequences of different densities, we have processed (16) high multiplicity events:

Cases	Efficiency	Purity	$\sigma_{r,\phi}(\mu m)$	$\sigma_z(\mu m)$	$\sigma_{de}(\%)$
$1-1$	97.6%	100.0%	13.4	750	4.2
$1-2$	94.8%	99.1%	34	1530	7.3
$2-2$	95.9%	94.8%	17.0	800	5.0
$2-3$	77.5%	94.6%	26	1220	8.1
$3-3$	76.4%	91.6%	20	800	5.6
Global	94.8%	98.8%	16.3	830	4.7

Table 7: Evaluation results (nominal noise, no dead strip): high multiplicity events.

Comparing them (10 hits per wafer) to standard ones, the global efficiency is of course lower because of the enhancement of the ambiguous cases but the value remains close to 95%. All the results show a global purity higher than 98% for the nominal level of noise.

Conclusion

The simulation part of the SSD software as well as the reconstruction chain and the evaluation procedure have been described in this work. For the reconstruction chain, methods based on charge-matching have been implemented in order to solve the space-point ambiguities. Its performance have been extensively tested by varying together the noise level with the dead strip rate, and by increasing the occupancy per detector from 5 hits up to 10 hits on the average. For nominal conditions of noise and strip defects, as given by in-beam test measurements, the efficiency and the purity are close to 96% and 99% respectively, while the position resolution in the bending plane ($r\phi$) is of about $16\mu m$.

References

[1] The STAR SVT Collaboration, Proposal for a Silicon Vertex Tracker (SVT) as un upgrade for the STAR experiment at RHIC, August 1994.

[2] Proposal for a Silicon Strip Detector for STAR, SN0400 June 1999.

[3] In-Beam test of double-sided silicon strip detector, L. Arnold et al, ALICE Note, INT-98-05.

[4] Off- and in-beam tests of Silicon-strip Detectors for the ALICE experiment at LHC, C. Suire et al, ALICE Note, INT-99-22.

[5] Performances of Double-Sided Silicon Strip Detectors for the ALICE experiment at LHC, F. Rétière et al, ALICE Note, INT-99-36.

[6] M. Germain et al, NIM **A434** (1999)345.

[7] Irradiation of a silicon-strip detector for the ALICE experiment at LHC, M. Germain et al, ALICE Note, INT-00-xx (to be published).

[8] Studies of ionizing Radiation Effects on Silicon Drift Detectors, S.U. Pandey et al, NIM **A361** (1995)457.

[9] Production tests, STAR Note to be published.